Progress In Electromagnetics Research, Vol. 177, 43–51, 2023

Broad-Tuning, Dichroic Metagrating Fabry-Perot Filter Based on Liquid Crystal for Spectral Imaging

Tingbiao Guo[1, 3, #], Zijian Lin[1, #], Xinan Xu[1], Zhi Zhang[1], Xiao Chen[1], Nan He[1], Guoqing Wang[2], Yi Jin[1], Julian Evans[1], and Sailing He[3, 1, *]

Abstract—Dynamic structural color can empower devices with additional functions like spectrum and polarization detection beyond display or imaging. However, present methods suffer from narrow tuning ranges, low throughput, or bulky volumes. In this work, a tunable filter composed of a dichroic metagrating Fabry-Perot cavity and liquid crystal (LC) material is proposed and investigated. By modulating the polarization of the incident light with the LC, the color response can change from blue to green and deep red due to the 'mode jumping' effect, with a tuning range of around 300 nm. Besides, we experimentally demonstrate the use of this device as a spectral imager in the visible range. Experimental results show that spectral resolvability can be around 10 nm, with the largest peak wavelength inaccuracy of ~ 5 nm. This approach shows superior performance over traditional liquid crystal tunable filters in low light conditions and indicates the potential of dynamic structural color for miniaturized spectroscopic applications.

1. INTRODUCTION

Functional metasurfaces have been demonstrated with exceptional degrees of freedom to manipulate lightwaves, ranging from beam deflectors [1], waveplates [2, 3], flat lenses [4], and holograms [5] to structural color [6–8] and absorber [9], among others. In many emerging scenarios like light detection and ranging (LiDAR) [10, 11], and virtual reality (VR) [12], dynamic control of the wavefront and amplitude is essential and necessary. However, most present metasurface devices are static with fixed functionality, hindering their employment for advanced applications. To overcome this limitation, efficient dynamic controlling mechanisms and materials like phase-change materials (PCM) [13], mechanical actuation [14, 15], carrier tuning [16] and liquid crystals (LCs) [17, 18] have been leveraged to enable metasurfaces with reconfigurable features. PCM or mechanical actuation mechanisms require cumbersome peripheral elements, and carrier tuning shows low modulation contrast, making the whole device heavy and low efficiency in the visible range.

Among these mechanisms, liquid crystal tuning is a promising approach for its high tuning efficiency, compactness and low driving voltage. It can be used to tune the response by either changing the refractive index of the surrounding environment or controlling polarization direction. By integrating liquid crystal with metasurfaces, dynamic color display [18, 19], transparent display [20], dynamic hologram [21], varifocal lens [22, 23] and phase-only modulators [24] have been proposed. However, the current tuning range of these devices is still limited to ~ 100 nm in the visible range, which severely restricts the usage for most applications, e.g., a single universal pixel for ultrahigh resolution color

Received 7 March 2023, Accepted 12 May 2023, Scheduled 25 May 2023

* Corresponding author: Sailing He (sailing@kth.se). # These authors contributed equally to this work.

[1] Centre for Optical and Electromagnetic Research, College of Optical Science and Engineering, National Engineering Research Center for Optical Instruments, Zhejiang University, Hangzhou 310058, China. [2] Zhejiang Suosi Technology Co. Ltd, Wenzhou 325000, Zhejiang, China. [3] Taizhou Hospital, Zhejiang University, Taizhou 318000, China.

display [25]. Additionally, most transmissive LC integrated-plasmonic devices have poor transmission, as most of the incident light is absorbed by the metals, which makes these devices energy-intensive [26, 27].

In this paper, we demonstrate a broad-tuning, dichroic filter by integrating a liquid crystal cell with a metagrating-based Fabry-Perot (MFP) cavity. By simply switching the input polarization with a liquid crystal retarder, the cavity can show two distinct transmissive colors from blue to red, spanning around 300 nm. The dichroism of the cavity originates from the metagrating that induces a phase difference for different polarization. And this large tuning range is a result of the 'mode jump' effect, where the response resonance switches from $TE_1(TM_0)$ to $TM_0(TE_1)$ mode when we change the input polarization. Due to the novel structures, the polarization transmission of our device can be around 50%, exceeding most metal-based devices. Combined with its broadband transmissive peak, the present filter supports a large optical throughput. As an example, we demonstrate spectral imaging using this dichroic color filter based on the computational reconstruction method. The present device shows spectral resolvability ~ 10 nm with the largest peak wavelength inaccuracy of ~ 5 nm and an average root mean square error of 0.056 for spectrum recovery. Owing to the large tuning range and high throughput, it outperforms traditional liquid crystal tunable filters in dark conditions. The excellent color fidelity between reconstructed and measured images suggests that it is a powerful tool in spectroscopy and other advanced applications, beyond display and imaging.

2. PRINCIPLE AND DESIGN

The proposed dichroic tunable filter is depicted in Figure 1. It is composed of an MFP cavity and an LC cell. The MFP cavity consists of thin silver (Ag) film on the bottom, a SiO_2 insulator layer in the middle, Ag metagratings as the top layer, and the photoresist of SU8 as the cladding layer. A parallel-aligned LC cell is laid above the MFP as a phase retarder. A polarizer is attached in front of the LC cell which is used as a polarization controller. For bare grating structures, no resonance exists, and hence the color fades. For the MFP, prominent peaks can be distinguished (see Section 1, Supporting Information). When applying a voltage on the LC cell, the input polarization can be altered and the resonant wavelength shifts. The tuning range due to the polarization switch can be up to ~ 300 nm in the visible region.

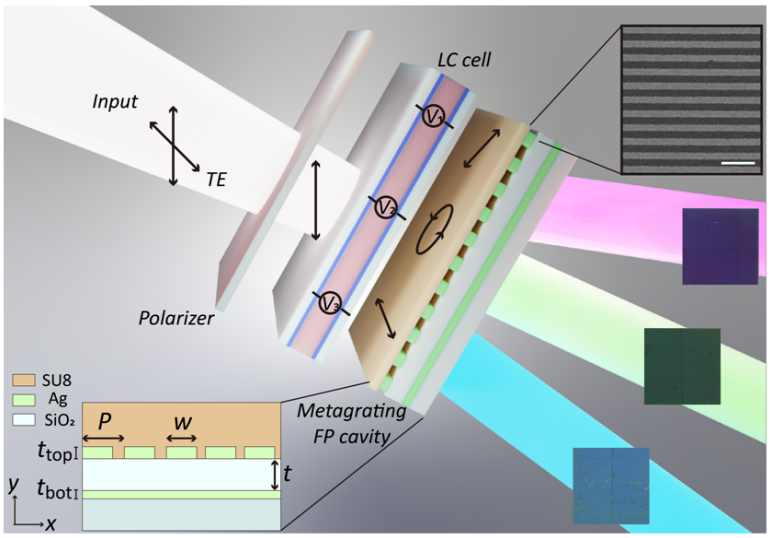

Figure 1. The schematic of the liquid crystal-driven metagrating FP cavity. Scale bar: 500 nm.

To understand the behavior of this device, we calculate the response of the device as the thickness of the insulator varies. In the calculation, the thickness of the top Ag layer $t_{top} = 50$ nm, the bottom Ag layer $t_{bot} = 15$ nm. The period P is set to 200 nm and the grating width w is 100 nm. Due to the birefringence of the metagrating, which causes a phase difference between two polarizations, the

resonant peaks split into two different branches for TE (E-component parallel with the grating) and TM input as shown in Figure 2(a). Compared with TE polarization, TM polarization experiences a smaller phase delay through the MFP (see Section 2, Supporting Information). As a result, a shorter resonant wavelength exists for TM input. And the wavelength difference is around 150 nm between the two polarizations for the same order.

As we increase the thickness of the insulator, both TE and TM resonances redshift to a longer wavelength. When reaching a proper thickness (dash line in Figures 2(a) and (b), $t = 230$ nm), for the TE input, the TE_1 mode occurs in the visible range while the TE_0 resonance shifts into the infrared regime. For TM polarization input, compared with the TE_0 resonance, the TM_0 resonance experiences a smaller optical path length, hence a shorter resonant wavelength. As a result, this resonance is still located in the visible range. That is, there only exist TE_1 and TM_0 modes in the visible band at this thickness. The theoretical results using the effective parameter retrieval method also fit well with these simulations (see Section 2, Supporting Information), clarifying the large anisotropy of the device [28]. In this case, the response resonance can shift from TE_1 mode (~ 450 nm) to the TM_0 mode (~ 750 nm) in the visible region, when varying input polarization from TE to TM, which we name as the 'mode jumping' effect. This wavelength shift (~ 300 nm) is twice larger than the shift between TE_0 and TM_0 resonances. To clarify this mode-switching nature, we also show the electric field distribution of the resonant modes labeled in Figure 2(b). There exist only one antinode for TM input and two antinodes for TE input, confirming the 'mode jumping' effect in the visible region (Figure 2(c)).

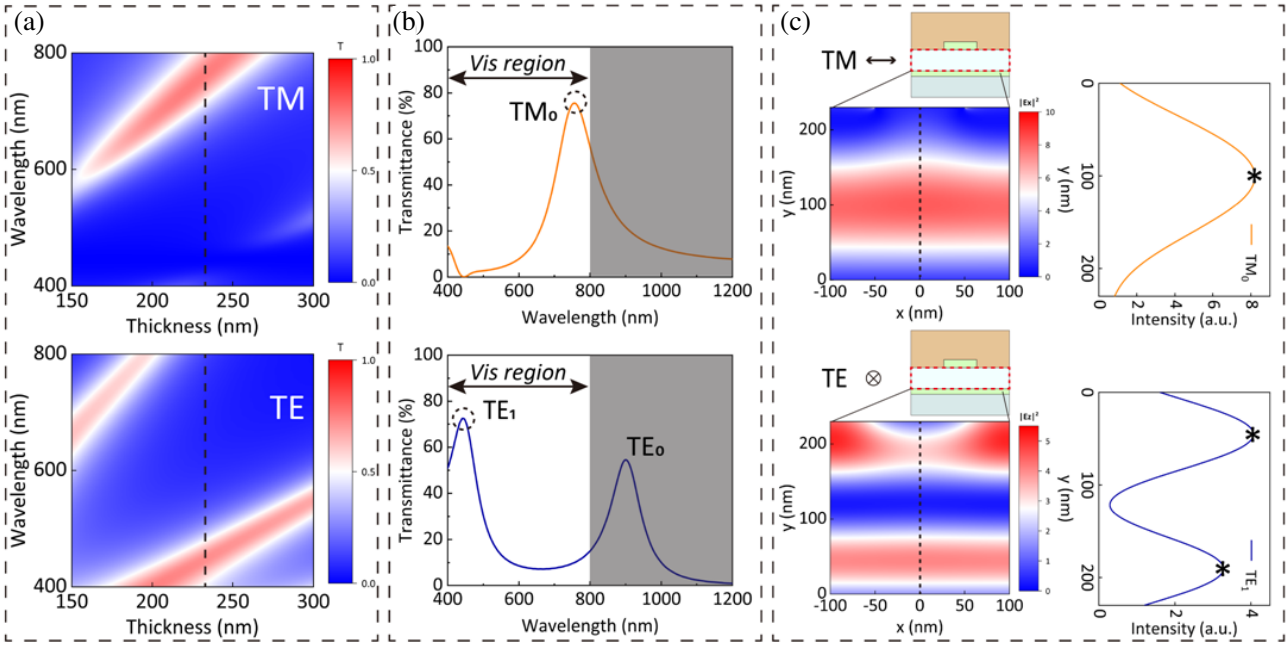

Figure 2. The simulation results for TE and TM input. (a) The response for TE and TM input with various insulator thicknesses. (b) The transmittance for TE and TM input for insulator thickness $t = 230$ nm (dashed lines in Figure 2(a)). (c) The mode profiles in the cavity for the corresponding modes labeled in Figure 2(b) by dashed circles. The antinodes is labeled as asterisks.

3. EXPERIMENT

The inset in Figure 1 shows the SEM image of the fabricated gratings. The thickness of the insulator is $t = 230$ nm. The measured geometric parameters are the same as the simulations. In Figure 3(a), we show the optical images and the corresponding transmissive spectra of the cavity. The resonance shift between two different polarization inputs can be ~ 300 nm, and the transmission for both polarizations

can be up to 50%, which is a huge improvement compared with other devices. Due to the large tuning range, the appearance color can change from blue to deep red for different polarizations, spanning the whole visible range. The experimental spectra fit well with the simulated ones, although the transmittance diminishes due to the surface roughness of the fabricated metals.

We then integrate the cavity with an LC cell. In this configuration, the LC cell is aligned with an anchoring layer in a parallel way, and the metagrating is perpendicular to the polarizer. Figure 3(b) shows the optical images and spectra after integrating the MFP with an LC cell. As can be seen from Figure 3(b), when a large voltage is applied to the LC cell, the incident light keeps TM polarization due to zero phase retardation of the LC cell. In this condition, the device shows a TM feature with resonance occurring at $\sim 750\,\text{nm}$. As we decrease the voltage, the retardation increases gradually. At ~ 4.1 and $\sim 2.3\,\text{V}$, due to the polarization transform of the LC cell, the device shows a TE feature with resonance located in the blue region ($\sim 450\,\text{nm}$). The largest wavelength shift is $\sim 300\,\text{nm}$ by the synergetic effect of the LC cell and the MFP. Given that the LC phase retarder (full waveplate) can transform the incident light from TM to any polarization, diverse spectra and colors (red, cyan, green and purple) can be obtained as the input voltage varies (Figure 3(b)). The output spectra can also be calculated by Jones calculus as shown below:

$$
\begin{aligned}
E_{out} &= \begin{bmatrix} E_{eout} \\ E_{mout} \end{bmatrix} = M_c \cdot R_2 \cdot M_{LC} \cdot R_1 \cdot E_{in} \\
&= \begin{bmatrix} T_e & 0 \\ 0 & T_m e^{i\delta} \end{bmatrix} \begin{bmatrix} \cos\beta & \sin\beta \\ \sin\beta & -\cos\beta \end{bmatrix} \begin{bmatrix} 1 & 0 \\ 0 & e^{i\delta_{LC}} \end{bmatrix} \begin{bmatrix} \cos\alpha & \sin\alpha \\ \sin\alpha & -\cos\alpha \end{bmatrix} \begin{bmatrix} E_{ein} \\ E_{min} \end{bmatrix}
\end{aligned} \tag{1}
$$

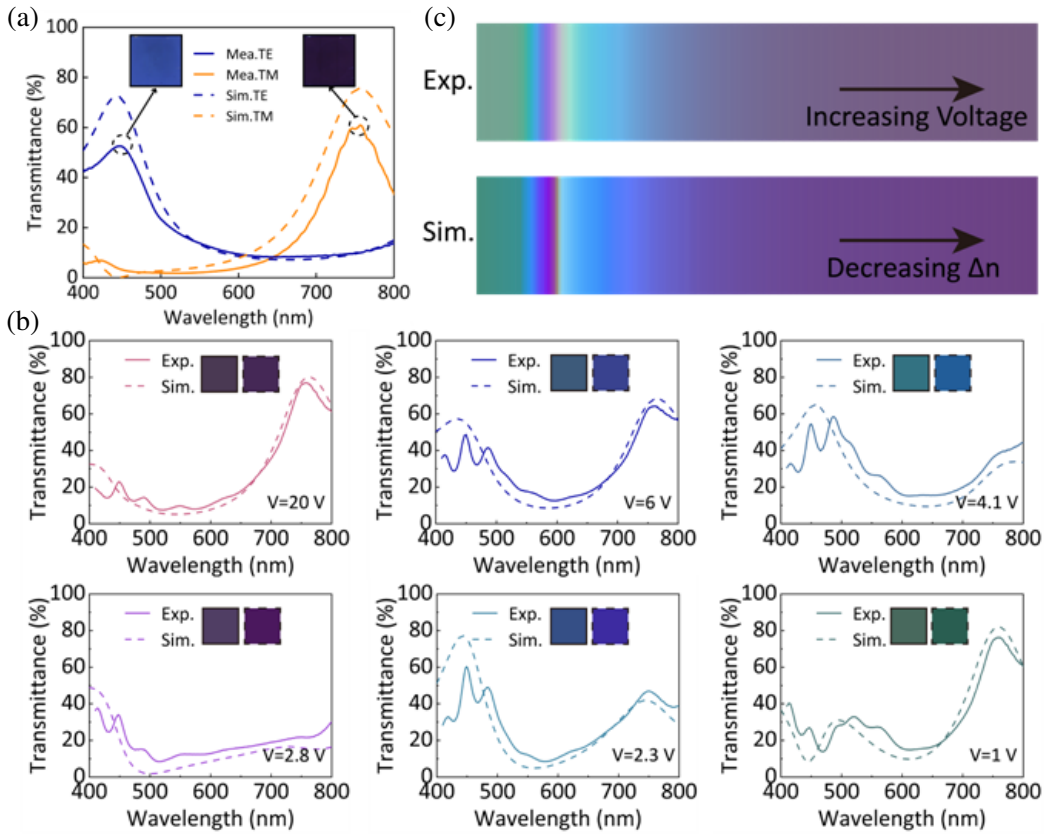

Figure 3. The color appearance and transmissive responses of the fabricated MFP filter. (a) The as-fabricated MFP without an LC cell. (b) The responses of the filter after integrating with an LC cell as the input voltage varies. (c) The simulated and measured colors as the phase retardation of the LC cell varies from 2π to 0 (voltage from 0 to 20 V).

where E_{eout} and E_{mout} are the TE and TM components of the output E_{out}, and E_{ein} and E_{min} are the TE and TM components of the input E_{in}. M_{LC} and M_c are the Jones matrix of the LC cell and the MFP. R_1 and R_2 are the rotation matrix. α and β are the angles between input light and LC director and LC director and metagratings. T_e and T_m are TE and TM transmittances of the MFP. δ is the phase delay between two polarizations for the MFP cavity. $\delta_{LC} = 2\pi\frac{\Delta nd}{\lambda}$ is the phase delay caused by the LC layer. $\Delta n = n_e - n_o$ is the refractive index difference of the LC material, which is controlled by the electric field. d and λ are the thickness of the LC layer and the wavelength of the incident light. Then the transmittance of the tunable filter T can be deduced as:

$$T = |E_{eout}|^2 + |E_{mout}|^2 \tag{2}$$

As we vary the input signals, δ_{LC} will change accordingly, hence the transmittance T will vary. The simulated output spectra and colors are shown in Figure 3(b) with the experimental ones. The calculated transmission curves fit well with the experimental results. The discrepancy may rise from the dispersion of birefringence as we used a linear birefringence model in the calculation (see Section 3, Supporting Information). Some ripples on the measured spectra can be due to the interference between the cladding, substrate, and LC cell. Colors at other voltages can be found in Supporting Information Section 4. By changing the geometric parameters, one can also tune the dichroism and hence control the transmittance response. As shown in Supporting Information Section 1, we show a simulated color table for various periods and duty cycles of the MFP and bare gratings. The color range of the proposed device can cover a large color gamut across the whole visible range.

Considering the dramatic spectrum modulation, we exploit this tunable filter for spectral imaging. In Supporting Information Section 5, we show the setup for spectral imaging. For the measurement, an LED light source with spectrum $I(\lambda_n)$ illuminates the objects. With the help of an objective and relay lens, the object is imaged on the intermediate image plane where we set the tunable filter. Another relay lens is then used to image both tunable filters and sample images on a black and white (B/W) camera. The responsivity of the camera is denoted as $S(\lambda_n)$. Then the measured intensity $P(V_m)$ for a single pixel can be calculated numerically as:

$$P\left(V_m\right) \approx \sum_{n=1}^{N} TF\left(V_m, \lambda_n\right) \times I\left(\lambda_n\right) \times S\left(\lambda_n\right) \times L\left(\lambda_n\right) \times R\left(\lambda_n\right), \quad m = 1...M \tag{3}$$

here, $R(\lambda_n)$ is the original spectrum to be measured. $TF(\lambda_n, V_m)$ is the transmission spectrum of the tunable filter at a voltage V_m. $L(\lambda_n)$ is the system response of the setup. N is the discrete wavelength channel that needs to be resolved. M defines the channel number of the tunable filter. Assuming that all pixels have the same responsivity $S(\lambda_n)$, then Equation (3) can be simplified as:

$$P\left(V_m\right) \approx \sum_{n=1}^{N} A\left(V_m, \lambda_n\right) \times R\left(\lambda_n\right), \quad m = 1...M \tag{4}$$

where $A(V_m, \lambda_n) = TF(V_m, \lambda_n) \times I(\lambda_n) \times S(\lambda_n) \times L(\lambda_n)$. The original spectrum $R(\lambda_n)$ can be reconstructed by solving a constrained linear least-squares problem of Equation (4).

We first measure a series of narrowband input signals with our tunable filter. Figure 4(a) shows the reference spectra (measured by a commercial spectrometer) and reconstructed spectra. Across the whole visible region, the recovered curves agree well with the reference spectra. The peak position can be precisely resolved with the largest inaccuracy of $\sim 5\,\text{nm}$ (Figures 4(b) and (c)). We also calculate the root mean square errors (RMSE) between the measured and reference spectra. The RMSE ranges between 0.015 and 0.114 with an average value of 0.056, which demonstrates a good reconstruction. The large discrepancy around 600 nm is due to the intersection of transmission spectra for different filter states, causing low-intensity contrast between tuning states. The filter is then used for spectral imaging of a colorful object. In the experiment, the spectra of each pixel are firstly reconstructed, then rendered to a post-colored image. Figures 4(d) and (e) show the original color pictures and the reconstructed images. While there are some color fading and noise, the whole picture looks the same as the original image. The noise may originate from the long-time exposure time (shot, thermal and fixed pattern noise) as the throughput is quite low due to the long optical path in the measurement. Figures 4(f) and (g) show the reflection spectra for color patches labeled in Figure 4(e). Spectra for other color

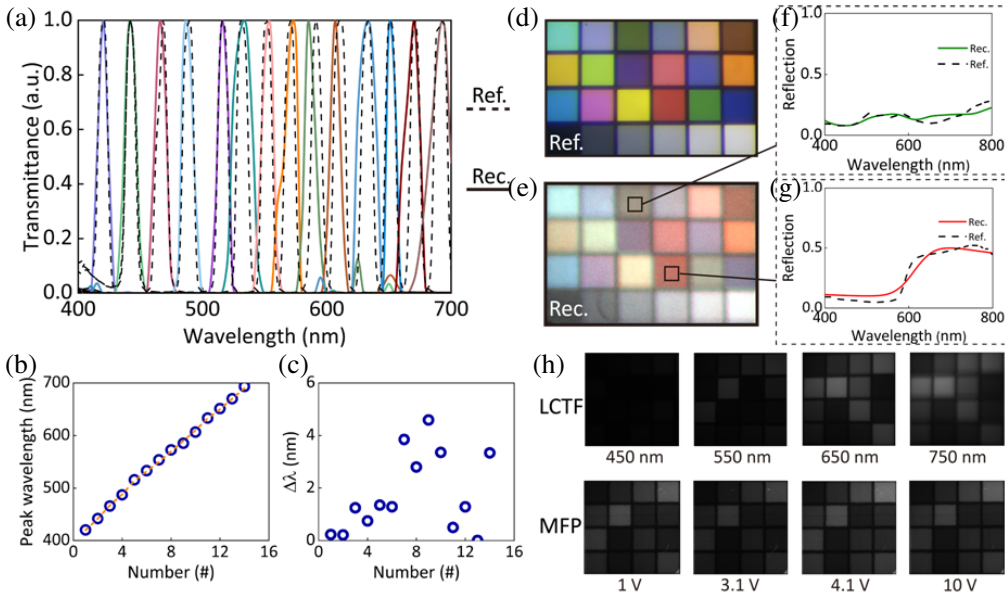

Figure 4. The spectral imaging demonstration by the present tunable filter via spectral scanning. (a) The reference (dashed lines) and recovered (solid lines) spectra for narrowband signals. (b) The peak wavelengths of the reconstructed and measured spectra. (c) The peak wavelength difference between reconstructed and reference spectra. (d) and (e) The reference image captured by a RGB camera and the reconstructed color image. (f) and (g) The reference and reconstructed spectra labeled in (e). (h) The B/W images captured by a commercial LCTF and our MFP.

patches can be found in Supporting Information Section 6. In Figure 4(h), we show the original B/W images captured by a commercial liquid crystal tunable filter (LCTF), which is commonly used as a spectral imager, and images captured by our filter in the same condition. The proposed tunable filter shows a higher optical throughput across the whole visible region, with an average signal power $\sim 40\%$ larger than LCTF, hence a better signal-to-noise ratio (see Supporting Information, Section 7). More importantly, the MFP keeps a more uniform power equalization across different channels as can be seen from Figure 4(h).

4. DISCUSSION AND CONCLUSION

In this work, we propose a broad-tuning dichroic filter by integrating an LC cell with a metagrating Fabry-Perot cavity. Due to the 'mode jumping' effect in this cavity, the resonant wavelength shift can reach around ~ 300 nm spanning the whole visible region, by varying the applied voltages on the LC cell. And by adjusting the geometric parameters of the cavity, the transmittances and colors can be tuned in a wide range. Taking the large tuning range and high transmittance ($\sim 50\%$), this design scheme offers a possible tool for achieving universal pixels in a dynamic display.

We also employ the filter for the advanced application of spectral imaging. Both narrow-band spectra and colorful objects can be reconstructed successfully through spectral scanning. Experimental results show that the spectral resolvability can be around 10 nm with a largest peak wavelength inaccuracy of ~ 5 nm. The RMSE between the measured and reference spectra is 0.056. The high transmittance and wide bandwidth of this filter ensure the system with high optical throughput and good power equalization, which benefits over commercial LCTF in low light conditions. It also shows superiority over a single LC cell-based spectral imager [29], as the correlation of each channel can be greatly reduced by inducing the metagrating cavity, which can lead to a thinner cell and faster response (see Section 8, Supporting Information). The performance comparison for other spectral imaging systems can be found in Supporting Information, Section 9. Our approach indicates the potential of present dynamic structural color filters for miniaturized spectroscopy applications like environmental

monitoring, drug screening and optical sorting.

5. METHOD

5.1. Simulation

To optimize the device performance, a finite difference time domain (FDTD) calculation is applied. For simplicity, we only simulate the response of the MFP, as the LC cell is only used as polarization control. In the simulation, the thickness of the bottom Ag layer is set to 15 nm. The top Ag grating thickness is 50 nm. The refractive index of silver is taken from the Handbook of Optical Constants of Solids [30], and the refractive index of the insulator is set as 1.46. The thickness of insulator t is fixed at 230 nm. The period P is set as 200 nm. The duty cycle is 0.5. The transmissive spectra after integrating LC are calculated following Equation (1) and Equation (2). $\delta_{LC} = 2\pi\frac{\Delta nd}{\lambda}$ is adopted from Thorlabs Inc. In the Jones calculus, $\alpha = \frac{\pi}{4}$ and $\beta = \frac{\pi}{2}$.

5.2. Fabrication

The device is fabricated via standard thin film deposition processes and E-beam lithography (EBL) techniques. A 15 nm Ag layer on a quartz substrate using DC sputtering is first deposited. A 230-nm SiO_2 thin film is then deposited by using plasma-enhanced chemical vapor deposition (PECVD). Afterward, the top grating pattern is produced by EBL and development. Subsequently, a 50 nm Ag layer is deposited by an e-beam evaporator, and then the lift-off process is conducted. Then, a thick SU8 layer is spun coated on the whole chip. A commercial LC retarder is then put onto the filter to control the polarization.

5.3. Measurement

The metagrating cavity with an LC cell is characterized by direct illumination of a white LED lamp and a spectrometer (Ocean Insight, QE Pro) on a customized system (see Section 5, Supporting Information), with 100 mV step from 0 to 20 volts. A signal generator (SIGLENT, SDG1062X) with square waves is used to drive the liquid crystal cell (THORLABS, LCC1413-A). For spectrum reconstruction, the B/W camera (ZWO, ASI432MM) is used to capture the intensity values of target objects at different voltages. Images are recorded with a homemade LabVIEW script. The narrowband spectra and color patches of the ColorChecker are measured with the commercial spectrometer directly to compare the accuracy of the spectral reconstruction. Finally, all data are processed with a homemade MATLAB script. The details for the reconstruction algorithm can be found in Section 10, Supporting Information.

DATA AVAILABILITY

All technical details for producing the figures are enclosed in the supplementary information. Data are available from the corresponding author upon reasonable request.

ACKNOWLEDGMENT

This work is partially supported by the "Pioneer" and "Leading Goose" R&D Program of Zhejiang (No. 2023C03083), the Zhejiang Provincial Natural Science Foundation of China (No. LY20H150008), the National Natural Science Foundation of China (Nos. 11621101 and 62105284), the National Key Research and Development Program of China (No. 2022YFB2804100), and the Special Development Fund of Shanghai Zhangjiang Science City, and Key Research and Development Program of Zhejiang Province (2021C03178).

CONFLICT OF INTEREST

A patent related to this work has been filed by T.B.G. and S.L.H. The authors declare no other conflict of interest.

REFERENCES

1. Yu, Y. F., A. Y. Zhu, R. Paniagua-Domínguez, Y. H. Fu, B. Luk'yanchuk, and A. I. Kuznetsov, "High-transmission dielectric metasurface with 2π phase control at visible wavelengths," *Laser & Photonics Reviews*, Vol. 9, 412–418, 2015.
2. Yu, N., F. Aieta, P. Genevet, M. A. Kats, Z. Gaburro, and F. Capasso, "A broadband, background-free quarter-wave plate based on plasmonic metasurfaces," *Nano Lett.*, Vol. 12, 6328–6333, 2012.
3. Ding, F., Z. Wang, S. He, V. M. Shalaev, and A. V. Kildishev, "Broadband high-efficiency half-wave plate: A supercell-based plasmonic metasurface approach," *ACS Nano*, Vol. 9, 4111–4119, 2015.
4. Khorasaninejad, M., W. T. Chen, R. C. Devlin, J. Oh, A. Y. Zhu, and F. Capasso, "Metalenses at visible wavelengths: Diffraction-limited focusing and subwavelength resolution imaging," *Science*, Vol. 352, 1190–1194, 2016.
5. Zheng, G., H. Mühlenbernd, M. Kenney, G. Li, T. Zentgraf, and S. Zhang, "Metasurface holograms reaching 80% efficiency," *Nature Nanotechnology*, Vol. 10, 308–312, 2015.
6. Kumar, K., H. Duan, R. S. Hegde, S. C. Koh, J. N. Wei, and J. K. Yang, "Printing colour at the optical diffraction limit," *Nature Nanotechnology*, Vol. 7, 557–561, 2012.
7. Cheng, F., J. Gao, T. S. Luk, and X. Yang, "Structural color printing based on plasmonic metasurfaces of perfect light absorption," *Scientific Reports*, Vol. 5, 11045, 2015.
8. Sun, S., Z. Zhou, C. Zhang, et al., "All-dielectric full-color printing with TiO_2 metasurfaces," *ACS Nano*, Vol. 11, 4445–4452, 2017.
9. Liu, N., M. Mesch, T. Weiss, M. Hentschel, and H. Giessen, "Infrared perfect absorber and its application as plasmonic sensor," *Nano Lett.*, Vol. 10, 2342–2348, 2010.
10. He, N., X. Xu, T. Guo, et al., "Highly compact all-solid-state beam steering module based on a metafiber," *ACS Photonics*, Vol. 9, 3094–3101, 2022.
11. Zhang, X., K. Kwon, J. Henriksson, J. Luo, and M. C. Wu, "A large-scale microelectromechanical-systems-based silicon photonics LiDAR," *Natur.*, Vol. 603, 253–258, 2022.
12. Lee, G.-Y., J.-Y. Hong, S.-H. Hwang, et al., "Metasurface eyepiece for augmented reality," *Nature Communications*, Vol. 9, 4562, 2018.
13. Abdollahramezani, S., O. Hemmatyar, M. Taghinejad, et al., "Dynamic hybrid metasurfaces," *Nano Lett.*, Vol. 21, 1238–1245, 2021.
14. Arbabi, E., A. Arbabi, S. M. Kamali, Y. Horie, M. Faraji-Dana, and A. Faraon, "MEMS-tunable dielectric metasurface lens," *Nature Communications*, Vol. 9, 812, 2018.
15. Meng, C., P. C. V. Thrane, F. Ding, et al., "Dynamic piezoelectric MEMS-based optical metasurfaces," *Science Advances*, Vol. 7, No. 26, eabg5639, 2021.
16. Huang, Y.-W., H. W. H. Lee, R. Sokhoyan, et al., "Gate-tunable conducting oxide metasurfaces," *Nano Lett.*, Vol. 16, 5319–5325, 2016.
17. Decker, M., C. Kremers, A. Minovich, et al., "Electro-optical switching by liquid-crystal controlled metasurfaces," *Opt. Express*, Vol. 21, 8879–8885, 2013.
18. Driencourt, L., F. Federspiel, D. Kazazis, et al., "Electrically tunable multicolored filter using birefringent plasmonic resonators and liquid crystals," *ACS Photonics*, Vol. 7, 444–453, 2019.
19. Franklin, D., R. Frank, S.-T. Wu, and D. Chanda, "Actively addressed single pixel full-colour plasmonic display," *Nature Communications*, Vol. 8, 15209, 2017.
20. Zou, C., A. Komar, S. Fasold, et al., "Electrically tunable transparent displays for visible light based on dielectric metasurfaces," *ACS Photonics*, Vol. 6, 1533–1540, 2019.
21. Kim, I., M. A. Ansari, M. Q. Mehmood, et al., "Stimuli-responsive dynamic metaholographic displays with designer liquid crystal modulators," *Adv. Mater.*, Vol. 32, 2004664, 2020.
22. Badloe, T., I. Kim, Y. Kim, J. Kim, and J. Rho, "Electrically tunable bifocal metalens with diffraction-limited focusing and imaging at visible wavelengths," *Advanced Science*, Vol. 8, 2102646, 2021.
23. Kobashi, J., H. Yoshida, and M. Ozaki, "Planar optics with patterned chiral liquid crystals," *Nature Photonics*, Vol. 10, 389–392, 2016.

24. Li, S.-Q., X. Xu, R. Maruthiyodan Veetil, V. Valuckas, R. Paniagua-Domínguez, and A. I. Kuznetsov, "Phase-only transmissive spatial light modulator based on tunable dielectric metasurface," *Science*, Vol. 364, 1087–1090, 2019.
25. Daqiqeh Rezaei, S., Z. Dong, J. Y. E. Chan, et al., "Nanophotonic structural colors," *ACS Photonics*, Vol. 8, 18–33, 2020.
26. Li, K., J. Wang, W. Cai, H. He, J. Liu, Z. Yin, D. Luo, Q. Mu, D. Gérard, and Y. J. Liu, "Electrically switchable structural colors based on liquid-crystal-overlaid aluminum anisotropic nanoaperture arrays," *Opt. Express*, Vol. 30, No. 18, 31913–31924, 2022.
27. Lee, Y., M.-K. Park, S. Kim, J. H. Shin, C. Moon, J. Y. Hwang, J.-C. Choi, H. Park, H.-R. Kim, and J. E. Jang, "Electrical broad tuning of plasmonic color filter employing an asymmetric-lattice nanohole array of metasurface controlled by polarization rotator," *ACS Photonics*, Vol. 4, 1954, 2017.
28. Smith, D., D. Vier, T. Koschny, and C. Soukoulis, "Electromagnetic parameter retrieval from inhomogeneous metamaterials," *Phys. Rev. E*, Vol. 71, No. 3, 036617, 2005.
29. August, I., Y. Oiknine, M. AbuLeil, I. Abdulhalim, and A. Stern, "Miniature compressive ultra-spectral imaging system utilizing a single liquid crystal phase retarder," *Scientific Reports*, Vol. 6, 1–9, 2016.
30. Palik, E. D., *Handbook of Optical Constants of Solids*, Academic Press, 1998.